Donor/π-Bridge Manipulation for Constructing a Stable NIR-II Aggregation-Induced Emission Luminogen with Balanced Phototheranostic Performance

Dingyuan Yan,[†,‡,§,#] Wei Xie,[†,‡,#] Jianyu Zhang,[§] Lei Wang,[†] Dong Wang,*[,†] and Ben Zhong Tang*[,§,‖]

[†]Center for AIE Research, College of Materials Science and Engineering, Shenzhen University, Shenzhen 518060, China.
[‡]College of Physics and Optoelectronic Engineering, Shenzhen University, Shenzhen 518060, China
[§]Hong Kong Branch of Chinese National Engineering Research Center for Tissue Restoration and Reconstruction, Department of Chemistry, Institute of Molecular Functional Materials, State Key Laboratory of Neuroscience, Division of Biomedical Engineering and Division of Life Science, The Hong Kong University of Science and Technology, Clear Water Bay, Kowloon, Hong Kong 999077, China.
[‖]Shenzhen Institute of Aggregate Science and Technology, School of Science and Engineering, The Chinese University of Hong Kong, Shenzhen, Guangdong 518172, China

ABSTRACT: Taking advantages of its versatile in functionality and tunable in dissipated energy equilibrium, aggregation-induced emission luminogens (AIEgens) become a rising star to offer multimodal theranostics platform as their easy-to-fabricated. Nevertheless, the construction of AIE-active phototheranostic agent in the second near-infrared window (NIR-II, 1000–1700 nm) which allows superior resolution and minimized photo damage is still a formidably challenging suffering from the limited candidate of building blocks. Herein, benzo[c]thiophene is firstly recommended as electron-rich and bulky donor (D)/π-bridge neighboring to the electron acceptor (A), which can enlarge the conjugation length as well distort the backbone. By precise D/π-bridge engineering, a stable NIR-II AIEgen DPBTA-DPTQ NPs with acceptable NIR-II fluorescence quantum yield of 0.45% and excellent photothermal conversion efficiency (PCE) of 40.6% under 808 nm laser irradiation is successfully obtained. Among the reported NIR-II AIEgens, the exactly spatial conformation of DPBTA-DPTQ is conformed for the first time by associating X-ray single crystal diffraction and theoretical simulations, elaborately revealing the relationship between structure and AIE effect/photothermal performance. Extensive tests in vitro demonstrate that the constructed NPs show efficient photothermal therapeutic effects. Benefiting from its outstanding performance in fluorescence imaging (FLI)/photoacoustic imaging (PAI)/photothermal imaging (PTI), trimodal imaging-guided photothermal eradication of tumor is performed in HepG2 and B16-F10 tumor-xenografted mice, demonstrating distinguished tumoricidal capability and good biocompatibility.

INTRODUCTION

Phototheranostic platforms, utilizing photoirradiation to enable simultaneous diseases diagnostics and therapeutics, emerge as an appealing toolbox in combinational cancer treatment by virtue of its noninvasive and controllable attributes.[1-5] Develop up to now, construction of multimodal phototheranostic system relies heavily on the combination of several components possessing separated individual attributes into an entirety, which is less accessible for clinical use on account of its complexity and poor repeatability.[6-8] With the rapid development of nanomedicine, effective one-for-all theranostic agents owing the integrated features of diagnostic and therapeutic functionalities simultaneously, are in highly and urgently demand yet a formidably tricky task arising from the competitive energy decay pathways upon photoexcitation.[9-11] On the basis of the Jablonski diagram, the photoexcited dyes can disperse the energy of excited state via radiative channel to provide fluorescence imaging (FLI) or nonradiative track to afford photoacoustic imaging (PAI)/ photothermal imaging (PTI)/photothermal therapy (PTT). Given the energy consumption is readily to happen through either of the two approaches spontaneously, there should be an adjustable platform which can finely regulate and balance these two processes in order to make the full usage of the excited-state energy, thus fulfilling multimodal imaging-guided phototherapy by using one single component.[12-14]
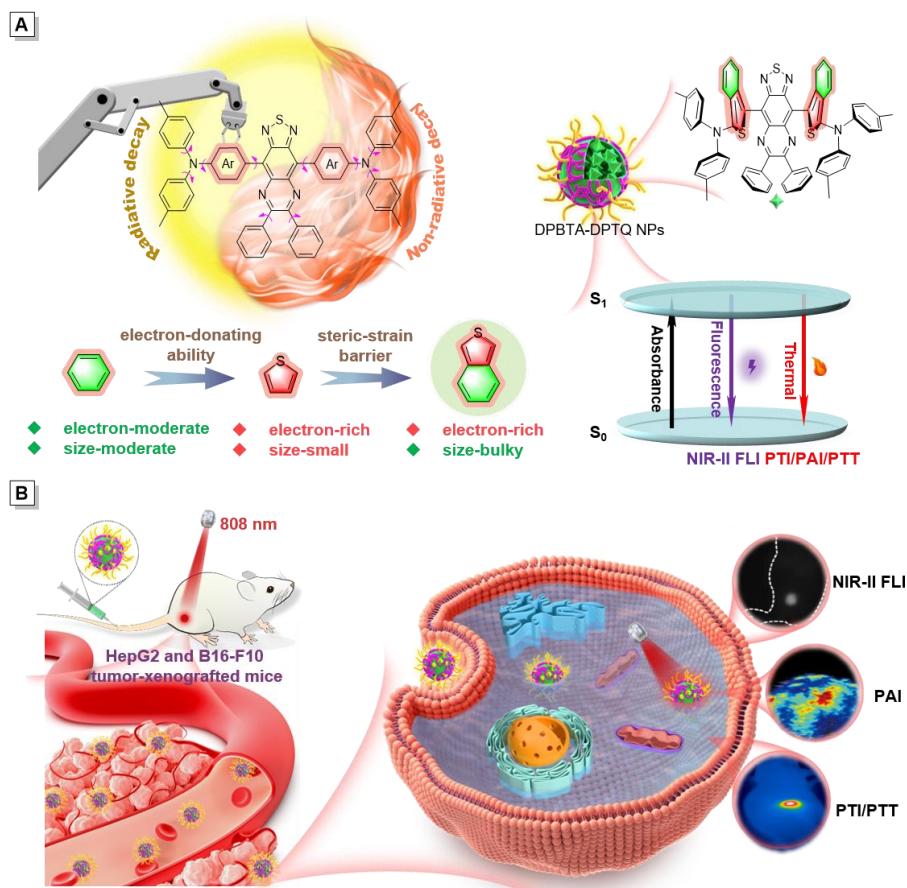
Figure 1. Schematic illustration of design principle, nanoparticles and versatile phototheranostic applications. (A) Molecular design philosophy for construction NIR-II AIEgen by D/π-bridge manipulation and illustration of the reconciled photophysical processes of DPBTA-DPTQ NPs after photoexcitation. (B) Application of DPBTA-DPTQ NPs on FLI/PAI/PTI trimodal imaging-guided cancer treatment.

With the merits of diminished photo scattering, negligible autofluorescence and deeper detection depth, optical imaging in the second near-infrared bio-window (NIR-II, 1000-1700 nm) which was pioneered by Dai and coworkers has explicitly demonstrated superior performance in vivo bioimaging, in comparison with the well-researched visible or NIR-I (700-900 nm) channels.[15-19] As compared with the inorganic NIR-II phototheranostic materials, organic counterparts are definitely appealing as their easy-to-fabricated, well-defined structure/purity, and prominent biodegradation/biocompatibility.[20-29] For constructing NIR-II organic luminescence, adjusting the extent of π-conjugation is a widely adopted protocol to extend fluorescence emission into the NIR-II region. Another accessible option is to link excessively strong electron-donating or withdrawing fragments into one single conjugated molecule, which can remarkably reduce the electronic bandgap. However, it is inevitable that those aromatic ring-fused structures tend to form clusters accompanied by intensely intermolecular π–π interactions in aqueous solution, leading to fairly weakened fluorescence emission. Fortunately, aggregation-induced emission (AIE), firstly coined by Tang *et al.*, offers an extremely powerful tool to circumvent this dilemma generating

from aggregation-caused quenching (ACQ) effect.[30-32] Unlike conventional chromophores which show dramatically decreased fluorescence signals in physiological environment, AIE luminogens (AIEgens) with flexibly propeller-like conformation emit particularly brightened fluorescence upon forming aggregates by reason of restriction of intramolecular motions (RIM) in return with boosting the energy radiative deactivation.[33,34] Additionally, for compounds consist of twisted backbone and flexible rotors, the dark twisted intramolecular charge transfer (TICT) state is favorable to access in polar solvent in which energy transition process can pour into nonradiative pathway to generate heat.[35,36] Moreover, donor (D)/acceptor (A) moieties incorporated in AIEgens could still reserve partial intramolecularly movement in the higher-order hierarchically distorted skeleton even in the aggregate state. Therefore, single element phototheranostic system with balanced radiative and nonradiative decays to meet multiple biomedical applications can be readily seized concurrently by the appropriate fabrication of AIEgens.[37-39]

Currently, the crucial prerequisite for obtaining NIR-II AIEgens is to distort the large π-delocalized backbone.[40,41] The most effective methods are to elevate the dihedral
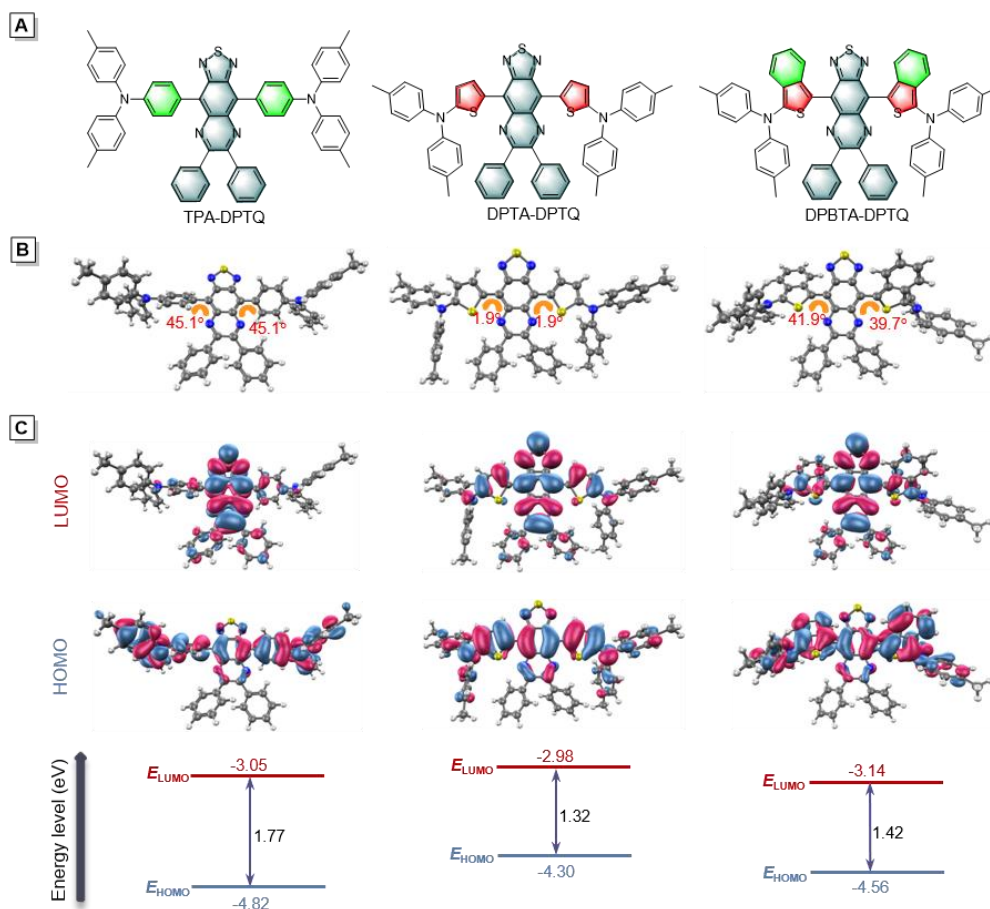
Figure 2. Structure details of TPA-DPTQ, DPTA-DPTQ and DPBTA-DPTQ. (A) Chemical structures. (B) Optimized S_0 geometries and (C) illustration of the frontier molecular orbitals (LUMOs and HOMOs) determined at the B3LYP/6-311g(d,p) level of theory.

angle between D/π-bridge and the adjacent A, or install shielding units encircling the molecule to cut down intermolecular stacking and prevent the interactions between the excited dyes with surrounding water.[19,42] In consideration of the limited choice of strong A, the incorporation of D/π-bridge with larger steric strain barrier is preferred to shape conformational distortion backbone. With this design philosophy, substituent manipulating aiming to endow classic electron-rich thiophene with crowded spatial restriction has been successfully applied. It is found that the introduce of congested 3,4-ethoxylene dioxythiophene (EDOT) or *ortho*-alkylated thiophene can increase the torsion angle between D/π-bridge and A as well as distort the conjugated backbone, thus boosting the fluorescence quantum yield (QY) in aggregate state.[43-45] By contrast, the bared thiophene or meta-alkylated thiophene can hardly constrain the reciprocal intermolecular interactions even further installing more distorted rotors.[46,47] Notwithstanding those intriguing advancement, much effort on developing novel D/π-bridge to enrich the library of NIR-II AIE theranostic agent deserves to be devoted. In this contribution, as illustrated in Figure 1A, we introduced a bulky electron-rich D/π-bridge block, benzo[c]thiophene, for the first time to develop high-performance D–π–A–π–D type NIR-II AIEgen by molecular engineering and uncover the relationship between the

structures and AIE characteristics/photothermal performance through the combination of theoretical simulation and X-ray single crystal diffraction. Furthermore, as-prepared DPBTA-DPTQ NPs displayed remarkable stability, excellent photothermal conversion capacity, and acceptable fluorescence QY in aqueous solution. Eventually, FLI/PAI/PTI trimodal imaging-guided PTT was carried out to eliminate tumor in HepG2 and B16-F10 tumor-xenografted mice, displaying predominant imaging and tumoricidal capability (Figure 1B).

RESULTS AND DISCUSSION

Molecular Design and Theoretical Calculation

Reinforcing the electron-donating ability of D or electron-withdrawing ability of A can dramatically contribute to the red-shifted absorption/emission wavelength. Compared to the frequently used coplanar electron acceptor core-benzobisthiadiazole (BBTD), 6,7-diphenyl-[1,2,5]thiadiazolo[3,4-g]quinoxaline (DPTQ) possesses the salient feature of a more congested geometry where two freely rotatable phenyl rings are covalently attached, which would be beneficial for achieving AIE activity.[48-50] However, the reported AIEgens based on DPTQ core can hardly emit the maximum emission beyond 1000 nm
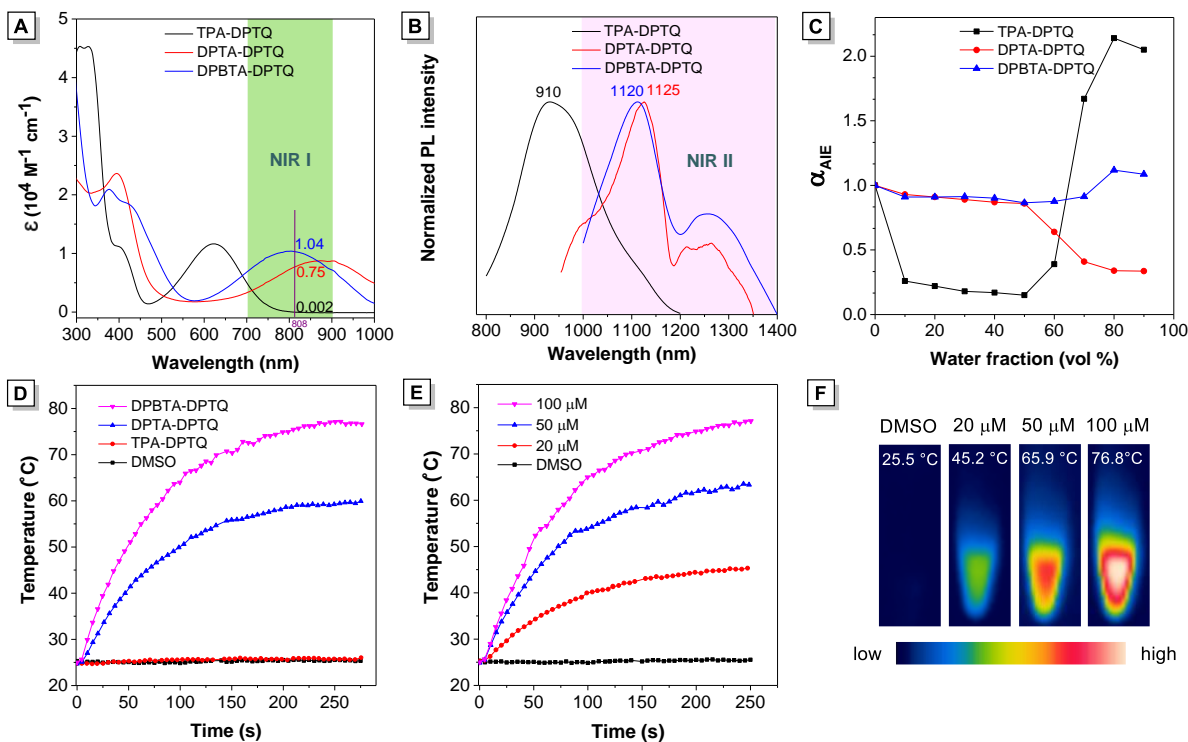
Figure 3. Characterizations and properties of the obtained compounds. (A) Absorption spectra and (B) normalized PL spectra of the compounds in THF solution (10 μM). (C) α_{AIE} value versus water fraction (f_w) in water/THF mixtures. α_{AIE} is defined as the ratio of the PL intensities of TPA-DPTQ at 910 nm, DPTA-DPTQ at 1125 nm and DPBTA-DPTQ at 1120 nm in water/THF mixtures and pure THF (f_w = 0). (D) Comparison of the photothermal conversion behavior of the compounds in DMSO solution (100 μM) under 808 nm laser irradiation. (E) Concentration-dependent temperature change of DPBTA-DPTQ in DMSO solution. (F) The corresponding IR thermal images under different conditions in Figure 3E at 4 min post-irradiation.

attribute to lack of strong electron donor/π-bridge. To explore suitable D/π-bridge segment, benzene, thiophene, and benzo[*c*]thiophene-bearing fragments were smoothly linked to DPTQ core through facile Buchwald-Hartwig or Stille cross-coupling reactions, yielding three molecules TPA-DPTQ, DPTA-DPTQ, and DPBTA-DPTQ with satisfying yields varying from 55% to 78% (Figure 2A, Scheme S1). The circumambient dimethylaniline serves not only as D to prolong the absorption/emission but also rotatable motors to convert thermal energy. All the intermediates and final products have been definitely confirmed by nuclear magnetic resonance (NMR) and high-resolution mass spectrum (HRMS) (Figures S1–S15). To explore more information about the structure conformation, optimized ground-state (S$_0$) geometries of the molecular was demonstrated by density functional theory calculations. For TPA-DPTQ, the two dihedral angles between the DPTQ core and its neighboring benzene rings are both 45.1°. If the benzene rings are replaced by thiophene rings which are smaller in size with decreased steric-resistance effect, the torsion angles reduced to 1.9°, forming nearly coplanar thiophene-DPTQ-thiophene center in DPTA-DPTQ. As for DPBTA-DPTQ, the introducing of benzo[*c*]thiophene which is a perfect integration of benzene and thiophene, distinctly enlarge the twisted extent between D/π-bridge and A to 41.9°/39.7° (Figure 2B). As displayed in Figure 2C, the electron cloud of the lowest un-

occupied molecular orbital (LUMO) of the chromophores is primarily distributed in the DPTQ core. While the highest occupied molecular orbital (HOMO) is delocalized across the whole conjugated backbone, revealing an apparent D–A interaction and intramolecular charge transfer effect from D/π-bridge to DPTQ core.

Photophysical Property and Photothermal Capacity Studies

Subsequently, the optical properties of the obtained fluorophores were characterized in THF solution. It was observed that they showed maximum absorption peaks at 623, 900, and 806 nm, with molar absorption coefficient (ε) of 0.002× 10^4, 0.75 × 10^4, and 1.04 × 10^4 M^{-1} cm^{-1} at 808 nm, respectively (Figure 3A). Ascribing to the incorporation of electron-rich thiophene and planarization of backbone, DPTA-DPTQ demonstrated substantial bathochromic shift both in absorption and emission in comparison with that of TPA-DPTQ. Although DPBTA-DPTQ showed blue-shifted absorption wavelength deriving from the breaking of coplanar geometry caused by the constrained benzo[*c*]thiophene unit, it showed emission maximum at 1120 nm which was similar with that of DPTA-DPTQ (Figure 3B). There are negligible changes in the absorption spectra when tested in different solvents. However, obvious decrease in PL emission intensity and red-shifted maximum wavelengths were detected with the increment of polarity originating from the twisted intra
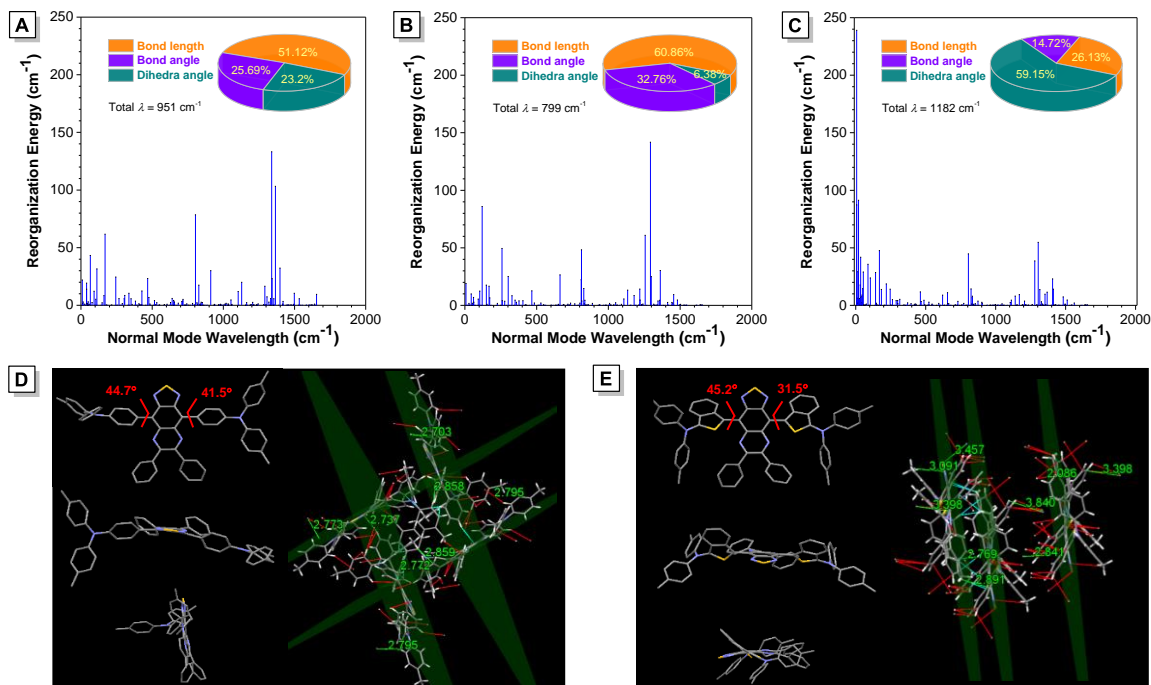
Figure 4. Calculated reorganization energy and X-ray single crystal diffraction studies. Calculated reorganization energy versus the normal mode wavenumbers of (A) TPA-DPTQ, (B) DPTA-DPTQ and (C) DPBTA-DPTQ. Insert graphs are the contribution to the total reorganization energy from the bond length, bond angle, and dihedral angle. Single crystal structure of (D) TPA-DPTQ and (E) DPBTA-DPTQ confirmed by single-crystal X-ray diffraction. Perspective view of molecular packing arrangement in crystals of TPA-DPTQ and DPBTA-DPTQ with intermolecular plane distances and various intermolecular and intramolecular interactions

molecular charge transfer (TICT) effect (Figure S16). The exploration of AIE attribute was subsequently implemented by using water/THF system with different water fractions. As expected, TPA-DPTQ exhibited prominent fluorescence enhancement with the increased ratio of water from 50% to 90%, behaving typical AIE effect. Whereas, obvious ACQ phenomenon with almost 70% discounted fluorescence intensity was observed when DPTA-DPTQ was examined, indicating the existence of extensive inter/intramolecular interactions. To our delight, the subtly modified larger steric-hindrance benzo[c]thiophene endowed DPBTA-DPTQ with capability to counteract the reduced brightness caused by the TICT effect in water, exhibiting weak AIE performance ultimately (Figure 3C, Figure S17). Subsequently, the photothermal behavior of the obtained luminescence was evaluated with an 808 nm laser (0.8 W cm^{-2}) in DMSO solution. The temperature of TPA-DPTQ solution remained neglectable change, which can be explained by the nearly zero light absorption under 808 nm. Upon 4 min continuously laser irradiation, temperatures of the DPTA-DPTQ and DPBTA-DPTQ solution reached to the plateau at 59.6 °C and 76.8 °C, respectively (Figure 3D). The better photothermal conversion effect of DPBTA-DPTQ partly resulted from its bigger absorption capacity (1.04 × 10^4 M^{-1} cm^{-1} of DPBTA-DPTQ versus 0.75 × 10^4 M^{-1} cm^{-1} of DPTA-DPTQ) at 808 nm (Figure 3E). Just as expected, DPBTA-

DPTQ solution displayed a conspicuous concentration-dependent temperature elevation (Figures 3E and 3F).

Calculated reorganization energy and X-ray single crystal diffraction studies

The calculated geometrical reorganization energy over the corresponding normal mode wavelength characterizes exhaustive details of the contribution of every mode of intramolecular motions to the non-radiative decay.[51] As shown in Figures 4B and 4C, the total reorganization energy of 1182 cm^{-1} in DPBTA-DPTQ is much higher than that of 799 cm^{-1} in DPTA-DPTQ, indicating stronger intramolecular motions of DPBTA-DPTQ. In addition, the high-frequency modes belonged to bond stretching with share of 93.62% prevail over the dihedral torsion with ratio of 6.38% in ACQ-active DPTA-DPTQ molecules, implying relative restrained backbone twisting motion. As for AIE-active DPBTA-DPTQ, the twisting of dihedral angle with a substantial part of 59.15% to the total reorganization energy mainly located in the low-frequency region (< 500 cm^{-1}). That means DPBTA-DPTQ may exhibit high potential of photothermal conversion ability upon photoexcitation. The single crystals of TPA-DPTA and DPBTA-DPTQ were successfully grown for deciphering their exactly spatial conformation and packing manner (Figure S18 and Table S1). As depicted in Figures 4D and 4E, the dihedral angles between the π-bridge and A were 44.7°/41.5° (for TPA-DPTQ) and 45.2°/31.5° (for DPBTA-DPTQ), respectively, which matched well with
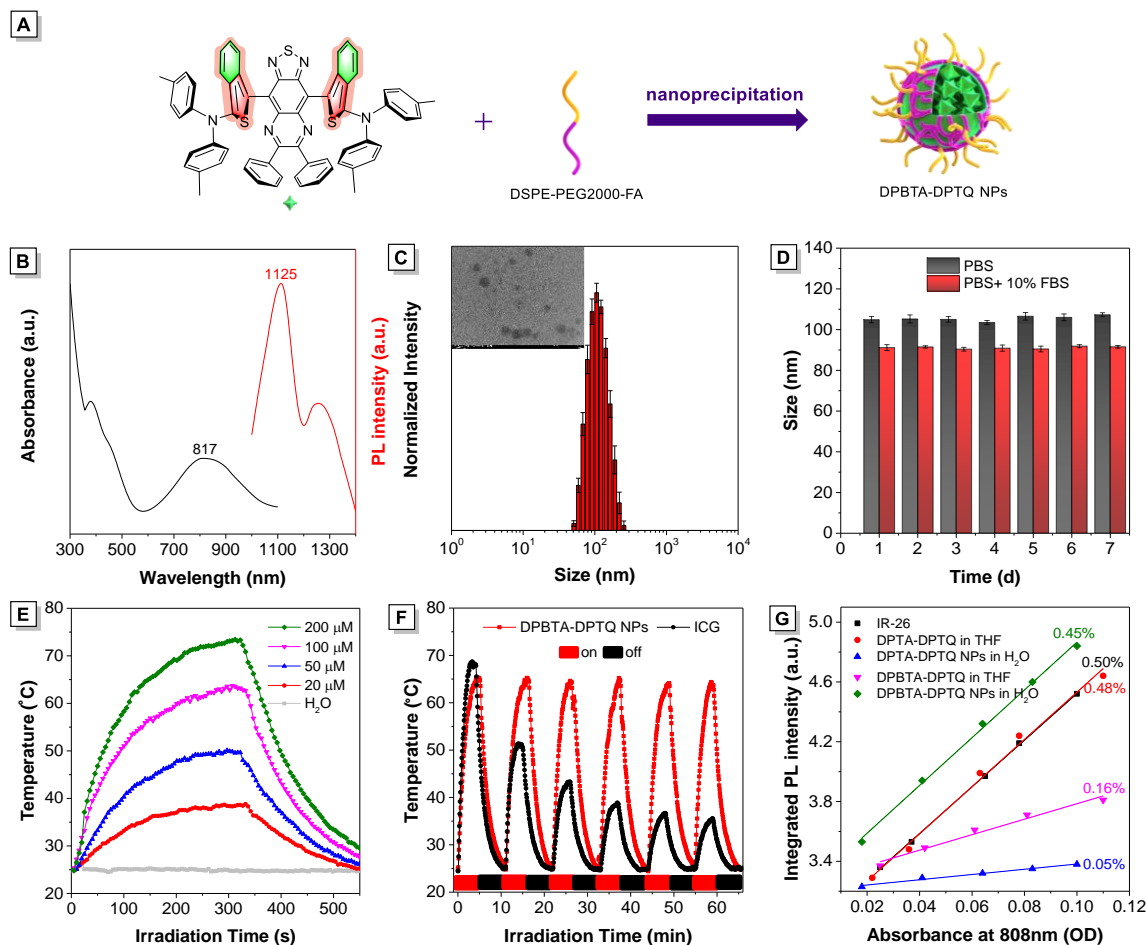
Figure 5. Characterization and properties of DPBTA-DPTQ NPs (A) Fabrication of DPBTA-DPTQ NPs by a nanoprecipitation method. (B) The absorption (blank line) and emission (red line) spectra of DPBTA-DPTQ NPs in aqueous solution. (C) DLS analysis of DPBTA-DPTQ NPs. Inset shows the TEM photograph of DPBTA-DPTQ NPs. (D) Stability analysis for size variation of DPBTA-DPTQ NPs with a concentration of 100 μM at room temperature in PBS or PBS + 10% FBS measured by DLS (means ± SD, n=3). (E) Photothermal conversion behavior of DPBTA-DPTQ NPs at different concentrations (20–200 μM) under 808 nm laser illumination. (F) Photothermal stability of DPBTA-DPTQ NPs and ICG (100 μM) in aqueous solution during six on/off irradiation cycles with an 808 nm laser. (G) The integrated fluorescence spectra (1000–1500 nm) of different state of the samples versus different absorbance at 808 nm (IR-26, QY = 0.5% in dichloroethane).

the theoretical simulated values. It is believed that the twisted molecular backbone and abundantly distributed inter- and intramolecular interactions (such as N···N, C–H···S, and C–H···π) in the crystal cells could efficaciously rigidify the structure framework and construct sterically constrained conformation, thus impeding the free movement of motors and turning out AIE behaviors. By carefully investigating the packing modes, we also observe that TPA-DPTQ packs in a much-disordered manner in its crystal phase where limited space for the free rotors is left. On the contrary, DPBTA-DPTQ is arranged in a roughly parallel fashion along the adjacent benzothiadiazole units, leading a looser packing way which is benign for dissipating excited energy via nonradiative deactivation and exhibiting a relatively weaker AIE property as aggregates.

Properties of DPBTA-DPTQ NPs

For the purpose of endowing the hydrophobic AIEgen with water-soluble property, DPBTA-DPTQ was fabricated into nanoparticles (NPs) through the ultrasound-assisted nanoprecipitation method by using an amphiphilic tumor specific co-polymer DSPE-PEG2000-FA (Figure 5A). UV–Vis–NIR absorption and fluorescence emission spectra of the DPBTA-DPTQ NPs showed negligible variations with its THF solution, locating at 817 nm and 1125 nm, respectively (Figure 5B). The encapsulated DPBTA-DPTQ NPs was well-dispersed in water with a diameter of ~105 nm measured by dynamic light scattering (DLS) and ~50 nm detected by transmission electron microscope (TEM) (Figure 5C). It is worth noticing that DPBTA-DPTQ NPs exhibited good stability when stored in PBS or 10% FBS solution at ambient condition for seven days, and slight change in absorption intensity was observed (Figure 5D, Figure S19). Whereafter, we quantitatively texted the photothermal performance of DPBTA-DPTQ NPs in aqueous solution upon exposure at 808 nm

wavelength. As illustrated in Figure 5E, after laser irradiation with power density value as 0.8 W cm^{-2} for 5 min, the temperature of 100 μM DPBTA-DPTQ NPs solution reached a plateau around 64 °C with a temperature elevation of 39 °C. An excellent photothermal conversion efficiency (η) of DPBTA-DPTQ NPs was determined to be 40.6 % based on the heating–cooling curve (Figure S20). Additionally, the photothermal behavior is positive correlated to the power of the laser and concentration of the NPs (Figure 5E, Figure S21). Noteworthily, the NPs reserved an outstanding photothermal stability after six continuously cyclic heating/cooling processes, whereas thermal conversion efficiency of indocyanine green (ICG) greatly reduced (Figure 5F). By using IR-26 as a reference, the QYs in the NIR-II region of DPTA-DPTQ and DPBTA-DPTQ in THF solution were determined to be 0.48% and 0.16% under 808 nm excitation, respectively. Notably, the QY of DPTA-DPTQ NPs dropped quickly to 0.005%, whereas that of DPBTA-DPTQ NPs increased almost two-fold to 0.45% which was higher than the well-studied 0.4% of carbon nanotubes[52] and 0.3% of CH1055-PEG[20] (Figure 5G, Figure S22).
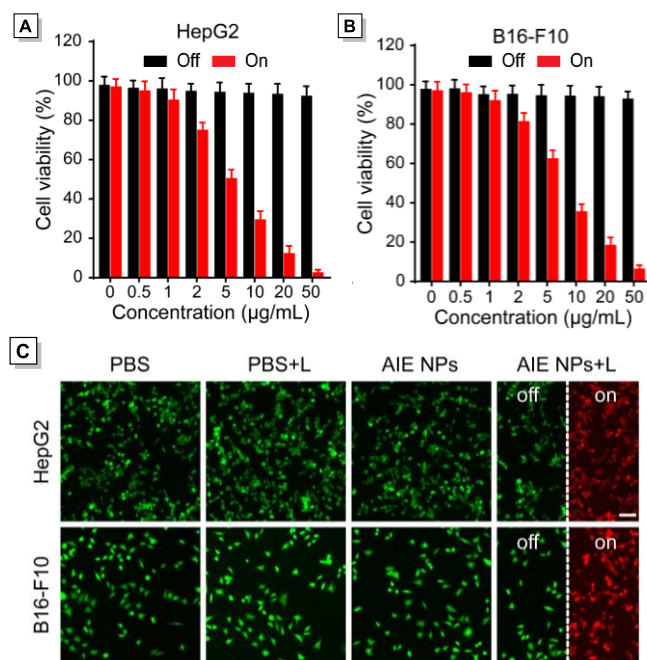
Figure 6. In vitro PTT cellular tumoricidal performance evaluation. Cell viability of (A) HepG2 cells and (B) B16-F10 cells after incubation with DPBTA-DPTQ NPs of different concentrations with or without 808 nm laser irradiation (0.8 W cm^{-2} for 7 min, n = 6, mean ± SD). Live/dead images of (C) HepG2 cells (upper row) and B16-F10 cells (lower row) after various treatments. AIE NPs on behalf of DPBTA-DPTQ NPs. The green fluorescence from FDA and red fluorescence from PI represent live cell and dead cell, respectively. Scale bar represents 50 μm.

In Vitro PTT Studies

To evaluate the dark cytotoxicity of DPBTA-DPTQ NPs in living normal cells, CCK-8 assay was used. There was no obvious decrease of the cell survival rate even when the RAW 264.7 cells were cultured at concentrations up to 50 μg mL^{-1} for 24 h, showcasing good biocompatibility (Figure S23). Considering its good photothermal behavior, the tumoricidal performance of DPBTA-DPTQ NPs towards HepG2 cells was further quantitatively assessed. Figure 6A showed minimal influence on the cell survival with a 92% cell viability under dark even in the presence of 50 μg mL^{-1} of DPBTA-DPTQ NPs, demonstrating low dark toxicity. However, in the presence of 808 nm (0.8 W cm^{-2}) irradiation by laser for 7 min, DPBTA-DPTQ NPs induced dose-dependent apoptosis. For the purpose of displaying photoablation effect of DPBTA-DPTQ NPs intuitively, live/dead cell staining was employed to differentiate live (green) and dead (red) HepG2 cells. After 7 min of irradiation, the fluorescence view of DPBTA-DPTQ NPs incubated HepG2 cells gradually turned from green to red, illuminating the death of cells (Figure 6C). By comparison, both laser and DPBTA-DPTQ NPs alone group was unable to kill cancer cells, which provide a further proof of biosecurity of DPBTA-DPTQ NPs without irradiation. Furthermore, the photokilling effect was firmly favored by DPBTA-DPTQ NPs treated B16-F10 cells under laser excitation, implying the feasible phototoxicity.

Imaging-Guided PTT in Vivo

Encouraged by the superior fluorescence property and in vitro phototherapeutic efficacy, in vivo multimodal imaging-guided therapy mediated by DPBTA-DPTQ NPs was subsequently evaluated. Figure 7A shows the procedure of mice experiment, in which tumors were inoculated and grew for 8 days before the execution of treatment. Fifteen days after treatment, the mice were sacrificed for analysis. Firstly, NIR-II FLI and PAI was accessed by intravenous administration of DPBTA-DPTQ NPs into HepG2 tumor-bearing BALB/c nude mice. As shown in Figures 7B and C, either NIR-II FLI or PAI displayed no signal before DPBTA-DPTQ NPs injection, suggesting minimal background signal. After intravenous injection of NPs, signal intensities of NIR-II FLI/PAI in the tumor section began to appear at 1 h and apparently increased along with time to a maximum level at 12 h, exhibiting prominent tumor-targeting ability of DPBTA-DPTQ NPs. At 24 h post-injection, the signals became gradually weaker, which might be due to the elimination of NPs from the body. In order to further survey the distribution of DPBTA-DPTQ NPs, the mice were sacrificed to investigate ex vivo NIR-II fluorescence signals of isolated tissues at 24 h post-injection. It was found that the tumor region exhibited obvious fluorescent signal even apparent signals were also detected in liver and kidney (Figure S24). Furthermore, in vivo PTI of DPBTA-DPTQ NPs was assessed by using 808 nm laser (0.8 W cm^{-2}) as a light source. After 12 h injection, infrared thermal images clearly visualized the rapid increase of temperature at the tumor site under laser illumination, rising from 36.5 °C to 50.1 °C within 2 min and stabilizing around 58.1 °C after 7 min period of exposure (Figure 7D). In the control group, the PBS-injected mice merely demonstrated slight temperature rise, illustrating the outstanding photothermal effi
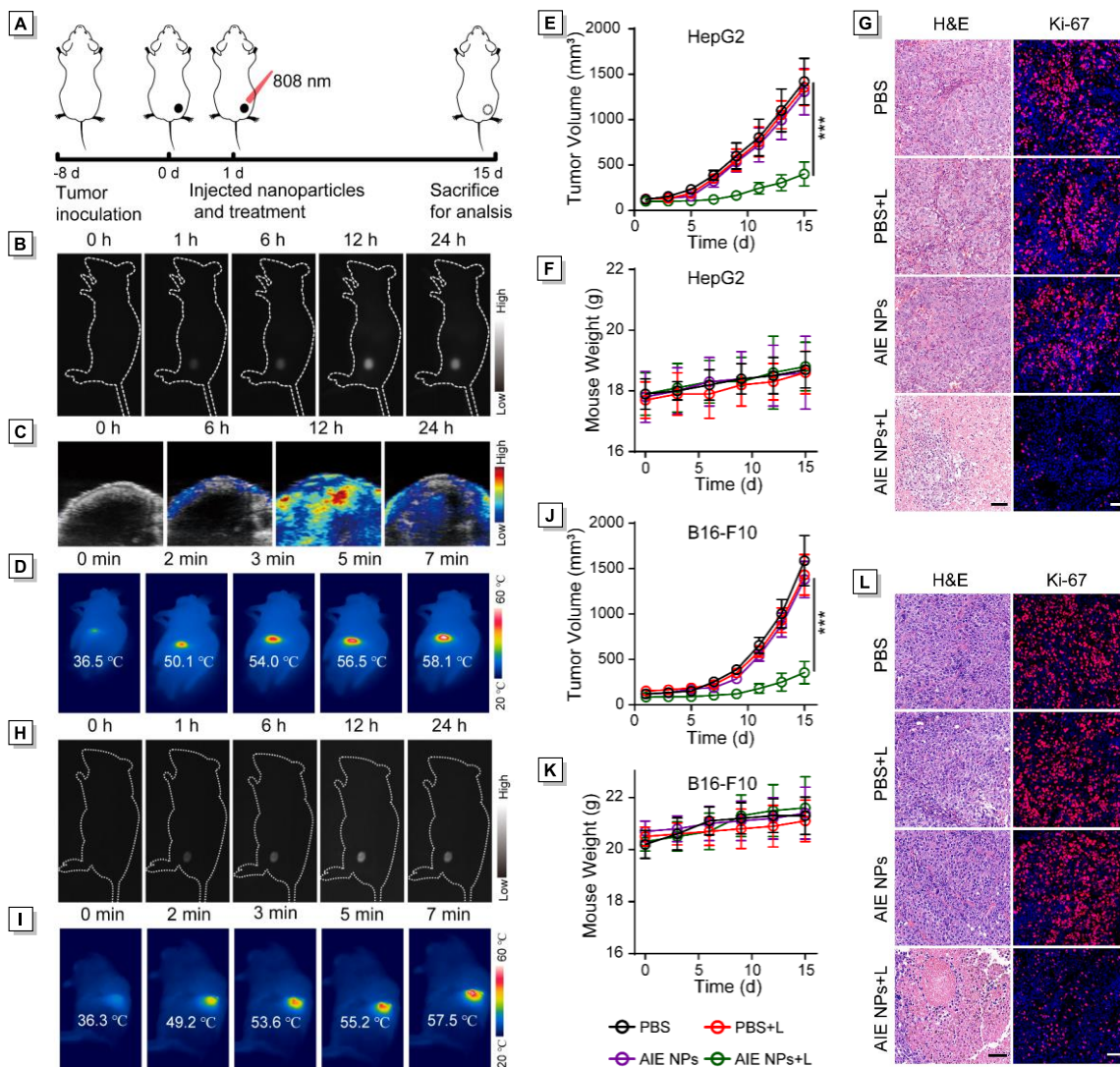
Figure 7. In vivo multimodal imaging-guided photothermal therapeutic efficiency of DPBTA-DPTQ NPs on HepG2 and B16-F10 tumor-bearing mice. (A) Schematic illustration of the treatment process to tumors. (B) NIR-II FLI, (C) PAI and (D) PTI of HepG2 tumor-bearing mice after intravenous injection of DPBTA-DPTQ NPs at different monitoring times. Time-dependent (E) tumor growth and (F) body weight curves of HepG2 tumor-bearing mice during the treatment process. (H) NIR-II FLI and (I) PTI of B16-F10 tumor-bearing mice after intravenous injection of DPBTA-DPTQ NPs at different monitoring times. Time-dependent (J) tumor growth and (K) body weight curves of B16-F10 tumor-bearing mice during the treatment process. Histological H&E and Ki67 staining analysis of (G) HepG2 tumor-bearing mice and (L) B16-F10 tumor-bearing mice tumor tissue under different treatment process. AIE NPs stand for DPBTA-DPTQ NPs. *** $P < 0.001$, n = 6. Scale bar: 100 μm.

-cacy of DPBTA-DPTQ NPs (Figure S25). Consequently, the trimodal NIR-II FLI/PAI/PTI by using a single component DPBTA-DPTQ NPs was verified to be feasible for improving the accuracy of diagnosis.

Later on, HepG2 tumor-bearing mice were randomly classified into four groups denoted as "PBS", "AIE NPs (abbreviation for DPBTA-DPTQ NPs)", "PBS + L (laser)", and "AIE NPs + L", respectively. In vivo PTT was conducted after 12 h tail vein injection of AIE NPs by using 808 nm laser illumination (0.8 W cm⁻²) for 7 min. As displayed in Figure 7E, the tumors displayed similar growth rates in the PBS, the laser only, and the NPs alone groups. However, for the group administrated with NPs plus laser showed distinct tumor growth inhibition in the next 15 d

post-treatment, manifesting significant tumoricidal efficiency. Additionally, the body weight profiles of all group showed similar growth tendency and no dead mice were found during the whole treatment period (Figure 7F). Afterward, we further conducted the antitumor effect by examining the tumor histological analysis (Figure 7G). By H&E analysis, apparent tumor necrosis area was observed in the group of "AIE NPs + L", keeping good agreement with the result of Ki67 immunofluorescence staining.

Furthermore, the thermal-ablation effect was further implemented in the B16-F10 tumor-xenografted C57BL/6 mice. The accumulation of the agent in tumor area was distinct visualized by NIR-II FLI/PTI bimodal imaging system after intravenous injection of AIE NPs (Figures 7H

and 7I). As expected, the phototherapeutic process which was similar with HepG2 tumor-bearing model exhibited distinguished performance. After treatment by AIE NPs and 808 nm laser irradiation, the growth of tumor was effectively suppressed and no apparent body weight loss was observed (Figures 7J–L).

As a promising biomedical therapeutic material, the in vivo biocompatibility of nanoparticles was examined systematically.[53] After intravenously injecting PBS or AIE NPs to healthy BALB/c nude mice for 30 days, the major organs of the mice were isolated for evaluation. As presented in Figure S26, no obvious variation in morphology of major organs were found in the H&E-staining slices of all group. In addition, blood biochemical parameters, including alanine transaminase (ALT), alkaline phosphatase (ALP), aspartate transaminase (AST), total blood urea nitrogen (BUN), and creatine (CRE) were collected and analyzed. All statistical analysis in the treated groups has no conspicuous adverse effect on the function of main organs (Figure S27).

CONCLUSIONS

In this contribution, molecular manipulation on the D/π-bridge segment is tactfully designed to construct a NIR-II AIEgen with high-performance phototheranostic ability. The introducing of a congested electron-rich benzo[c]thiophene unit endows DPBTA-DPTQ with a twisted conformation which is beneficial to prolong absorption/emission wavelength as well as obtain high QY by preventing notorious π-π stacking in aggregates. Besides, movable rotators and vibrators enable DPBTA-DPTQ with high heat conversion behavior. The structure-property relationship of the obtained fluorophores is fully illuminated by the comprehensive integration of theoretical simulation and X-ray single crystal diffraction. Benefitting from these notable features, trimodal NIR-II FLI/PAI/PTI imaging-guided photothermal ablation of tumor is executed in HepG2 tumor-bearing mice in vitro and in vivo, showcasing significant therapeutic efficiency and biocompatibility. Moreover, the successful therapeutic effect in B16-F10 tumor-bearing immune-competent mice breed new possibility of PTT potentiated immunotherapy.[54,55] Undoubtedly, this work will bring an innovative guideline to design multifunctional NIR-II AIEgens, rendering great promise of building high-performance all-in-one phototheranostic agent.

ASSOCIATED CONTENT

Supporting Information. General information about materials and methods, synthesis and characterizations, NMR spectra of the compounds. This material is available free of charge via the Internet at http://pubs.acs.org.

AUTHOR INFORMATION

Corresponding Author
*wangd@szu.edu.cn
*tangbenz@ust.hk

Author Contributions
#D. Yan and W. Xie contributed equally to this work.

REFERENCES
(1) Ng, K. K.; Zheng, G. Molecular Interactions in Organic Nanoparticles for Phototheranostic Applications. *Chem. Rev.* **2015**, *115*, 11012-11042.

(2) Chen, H.; Zhang, W.; Zhu, G.; Xie, J.; Chen, X. Rethinking cancer nanotheranostics. *Nat. Rev. Mater.* **2017**, *2*, 17024.

(3) He, S.; Song, J.; Qu, J.; Cheng, Z. Crucial breakthrough of second near-infrared biological window fluorophores: design and synthesis toward multimodal imaging and theranostics. *Chem. Soc. Rev.* **2018**, *47*, 4258-4278.

(4) Qi, J.; Ou, H.; Liu, Q.; Ding, D. Gathering brings strength: How organic aggregates boost disease phototheranostics. *Aggregate* **2021**, *2*, 95-113.

(5) Smith, B. R.; Gambhir, S. S. Nanomaterials for In Vivo Imaging. *Chem. Rev.* **2017**, *117*, 901-986.

(6) Huang, J.; He, B.; Zhang, Z.; Li, Y.; Kang, M.; Wang, Y.; Li, K.; Wang, D.; Tang, B. Z. Aggregation-Induced Emission Luminogens Married to 2D Black Phosphorus Nanosheets for Highly Efficient Multimodal Theranostics. *Adv. Mater.* **2020**, *32*, 2003382.

(7) Fan, W.; Yung, B.; Huang, P.; Chen, X. Nanotechnology for Multimodal Synergistic Cancer Therapy. *Chem. Rev.* **2017**, *117*, 13566-13638.

(8) Feng, W.; Han, X.; Wang, R.; Gao, X.; Hu, P.; Yue, W.; Chen, Y.; Shi, J. Nanocatalysts-Augmented and Photothermal-Enhanced Tumor-Specific Sequential Nanocatalytic Therapy in Both NIR-I and NIR-II Biowindows. *Adv. Mater.* **2019**, *31*, 1805919.

(9) Zhang, Z.; Xu, W.; Kang, M.; Wen, H.; Guo, H.; Zhang, P.; Xi, L.; Li, K.; Wang, L.; Wang, D.; Tang, B. Z. An All-Round Athlete on the Track of Phototheranostics: Subtly Regulating the Balance between Radiative and Nonradiative Decays for Multimodal Imaging-Guided Synergistic Therapy. *Adv. Mater.* **2020**, *32*, 2003210.

(10) Kang, M.; Zhou, C.; Wu, S.; Yu, B.; Zhang, Z.; Song, N.; Lee, M. M. S.; Xu, W.; Xu, F. J.; Wang, D.; Wang, L.; Tang, B. Z. Evaluation of Structure-Function Relationships of Aggregation-Induced Emission Luminogens for Simultaneous Dual Applications of Specific Discrimination and Efficient Photodynamic Killing of Gram-Positive Bacteria. *J. Am. Chem. Soc.* **2019**, *141*, 16781-16789.

(11) Xu, W.; Lee, M. M. S.; Nie, J. J.; Zhang, Z.; Kwok, R. T. K.; Lam, J. W. Y.; Xu, F. J.; Wang, D.; Tang, B. Z. Three-Pronged Attack by Homologous Far-red/NIR AIEgens to Achieve 1+1+1>3 Synergistic Enhanced Photodynamic Therapy. *Angew. Chem. Int. Ed.* **2020**, *59*, 9610.

(12) Kang, M.; Zhang, Z.; Song, N.; Li, M.; Sun, P.; Chen, X.; Wang, D.; Tang, B. Z., Aggregation - enhanced theranostics: AIE Sparkles in Biomedical Field. *Aggregate* **2020**, *1*, 80-106.

(13) Li, L.; Shao, C.; Liu, T.; Chao, Z.; Chen, H.; Xiao, F.; He, H.; Wei, Z.; Zhu, Y.; Wang, H.; Zhang, X.; Wen, Y.; Yang, B.; He, F.; Tian, L. An NIR-II-Emissive Photosensitizer for Hypoxia-Tolerant Photodynamic Theranostics. *Adv. Mater.* **2020**, *32*, 2003471.

(14) Gao, S.; Yu, S.; Zhang, Y.; Wu, A.; Zhang, S.; Wei, G.; Wang, H.; Xiao, Z.; Lu, W., Molecular Engineering of Near‐Infrared‐II Photosensitizers with Steric‐Hindrance Effect for Image‐Guided Cancer Photodynamic Therapy. *Adv. Funct. Mater.* **2021**, *31*, 2008356.

(15) Hong, G; Antaris, A. L.; Dai, H., Near-infrared fluorophores for biomedical imaging. *Nat. Biomed. Eng* **2017**, *1*, 0010.

(16) Li, C.; Chen, G.; Zhang, Y.; Wu, F.; Wang, Q., Advanced Fluorescence Imaging Technology in the Near-Infrared-II Window for Biomedical Applications. *J. Am. Chem. Soc.* **2020**, *142*, 14789-14804.

(17) Yin, C.; Lu, X.; Fan, Q.; Huang, W. Organic semiconducting nanomaterials‐assisted phototheranostics in near‐infrared‐II biological window. *View* **2020**, *2*, 20200070.

(18) Yang, Q.; Ma, H.; Liang, Y.; Dai, H. Rational Design of High Brightness NIR-II Organic Dyes with S-D-A-D-S Structure. *Acc. Mater. Res.* **2021**, *2*, 170-183.

(19) Hong, G.; Zou, Y.; Antaris, A. L.; Diao, S.; Wu, D.; Cheng, K.; Zhang, X.; Chen, C.; Liu, B.; He, Y.; Wu, J. Z.; Yuan, J.; Zhang, B.; Tao, Z.; Fukunaga, C.; Dai, H. Ultrafast fluorescence imaging in vivo with conjugated polymer fluorophores in the second near-infrared window. *Nat. Commun.* **2014**, *5*, 4206.

(20) Antaris, A. L.; Chen, H.; Cheng, K.; Sun, Y.; Hong, G.; Qu, C.; Diao, S.; Deng, Z.; Hu, X.; Zhang, B.; Zhang, X.; Yaghi, O. K.; Alamparambil, Z. R.; Hong, X.; Cheng, Z.; Dai, H. A small-molecule dye for NIR-II imaging. *Nat. Mater.* **2016**, *15*, 235-42.

(21) Zhang, X. D.; Wang, H.; Antaris, A. L.; Li, L.; Diao, S.; Ma, R.; Nguyen, A.; Hong, G.; Ma, Z.; Wang, J.; Zhu, S.; Castellano, J. M.; Wyss-Coray, T.; Liang, Y.; Luo, J.; Dai, H. TraμMatic Brain Injury Imaging in the Second Near-Infrared Window with a Molecular Fluorophore. *Adv. Mater.* **2016**, *28*, 6872-6879.

(22) Yang, Q.; Ma, Z.; Wang, H.; Zhou, B.; Zhu, S.; Zhong, Y.; Wang, J.; Wan, H.; Antaris, A.; Ma, R.; Zhang, X.; Yang, J.; Zhang, X.; Sun, H.; Liu, W.; Liang, Y.; Dai, H. Rational Design of Molecular Fluorophores for Biological Imaging in the NIR-II Window. *Adv. Mater.* **2017**, *29*, 1605497.

(23) Li, B.; Lu, L.; Zhao, M.; Lei, Z.; Zhang, F. An Efficient 1064 nm NIR-II Excitation Fluorescent Molecular Dye for Deep-Tissue High-Resolution Dynamic Bioimaging. *Angew. Chem. Int. Ed.* **2018**, *57*, 7483-7487.

(24) Kenry; Duan, Y.; Liu, B. Recent Advances of Optical Imaging in the Second Near-Infrared Window. *Adv. Mater.* **2018**, *30*, 1802394.

(25) Wan, H.; Yue, J.; Zhu, S.; Uno, T.; Zhang, X.; Yang, Q.; Yu, K.; Hong, G.; Wang, J.; Li, L.; Ma, Z.; Gao, H.; Zhong, Y.; Su, J.; Antaris, A. L.; Xia, Y.; Luo, J.; Liang, Y.; Dai, H. A bright organic NIR-II nanofluorophore for three-dimensional imaging into biological tissues. *Nat. Commun.* **2018**, *9*, 1171.

(26) Sun, C.; Li, B.; Zhao, M.; Wang, S.; Lei, Z.; Lu, L.; Zhang, H.; Feng, L.; Dou, C.; Yin, D.; Xu, H.; Cheng, Y.; Zhang, F. J-Aggregates of Cyanine Dye for NIR-II in Vivo Dynamic Vascular Imaging beyond 1500 nm. *J. Am. Chem. Soc.* **2019**, *141*, 19221-19225.

(27) Zhu, S.; Tian, R.; Antaris, A. L.; Chen, X.; Dai, H., Near-Infrared-II Molecular Dyes for Cancer Imaging and Surgery. *Adv. Mater.* **2019**, *31*, 1900321.

(28) Huang, J.; Xie, C.; Zhang, X.; Jiang, Y.; Li, J.; Fan, Q.; Pu, K. Renal-clearable Molecular Semiconductor for Second Near-Infrared Fluorescence Imaging of Kidney Dysfunction. *Angew. Chem. Int. Ed.* **2019**, *58*, 15120-15127.

(29) Zhang, F.; Chen, Y.; Pei, P.; Lei, Z.; Zhang, X.; Yin, D. A Promising NIR-II Fluorescent Sensor for Peptide-Mediated

Long-term Monitoring of Kidney Dysfunction. *Angew. Chem. Int. Ed.* **2021**, 10.1002/anie.202103071.

(30) Mei, J.; Hong, Y.; Lam, J. W.; Qin, A.; Tang, Y.; Tang, B. Z. Aggregation-induced emission: the whole is more brilliant than the parts. *Adv. Mater.* **2014**, *26*, 5429-5479.

(31) Mei, J.; Leung, N. L.; Kwok, R. T.; Lam, J. W.; Tang, B. Z. Aggregation-Induced Emission: Together We Shine, United We Soar! *Chem. Rev.* **2015**, *115*, 11718-940.

(32) Wang, D.; Tang, B. Z. Aggregation-Induced Emission Luminogens for Activity-Based Sensing. *Acc. Chem. Res.* **2019**, *52*, 2559–2570.

(33) Tang, B. Z.; Zhao, Z.; Zhang, H.; Lam, J. W. Y. Aggregation-Induced Emission: New Vistas at Aggregate Level. *Angew. Chem. Int. Ed.* **2020**, *59*, 9888.

(34) Yan, D., Wu, Q., Wang, D. and Tang, B.Z. Innovative Synthetic Procedures for Luminogens Showing Aggregation-Induced Emission. *Angew. Chem. Int. Ed.* **2021**, 10.1002/anie.20200619.

(35) Liu, S.; Zhou, X.; Zhang, H.; Ou, H.; Lam, J. W. Y.; Liu, Y.; Shi, L.; Ding, D.; Tang, B. Z. Molecular Motion in Aggregates: Manipulating TICT for Boosting Photothermal Theranostics. *J. Am. Chem. Soc.* **2019**, *141*, 5359-5368.

(36) Liu, S.; Li, Y.; Zhang, H.; Zhao, Z.; Lu, X.; Lam, J. W. Y. Tang, B. Z., Molecular Motion in the Solid State. *ACS Materials Lett.* **2019**, *1*, 425-431.

(37) Zhu, W.; Kang, M.; Wu, Q.; Zhang, Z.; Wu, Y.; Li, C.; Li, K.; Wang, L.; Wang, D.; Tang, B. Z. Zwitterionic AIEgens: Rational Molecular Design for NIR‐II Fluorescence Imaging‐Guided Synergistic Phototherapy. *Adv. Funct. Mater.* **2020**, *31*, 2007026.

(38) Gao, S.; Wei, G.; Zhang, S.; Zheng, B.; Xu, J.; Chen, G.; Li, M.; Song, S.; Fu, W.; Xiao, Z.; Lu, W. Albumin tailoring fluorescence and photothermal conversion effect of near-infrared-II fluorophore with aggregation-induced emission characteristics. *Nat. Commun.* **2019**, *10*, 2206.

(39) Xu, Y.; Zhang, Y.; Li, J.; An, J.; Li, C.; Bai, S.; Sharma, A.; Deng, G.; Kim, J. S.; Sun, Y. NIR-II emissive multifunctional AIEgen with single laser-activated synergistic photodynamic/photothermal therapy of cancers and pathogens. *Biomaterials* **2020**, *259*, 120315.

(40) Liu, S.; Li, Y.; Kwok, R. T. K.; Lam, J. W. Y.; Tang, B. Z. Structural and process controls of AIEgens for NIR-II theranostics. *Chem. Sci.* **2020**, *12*, 3427–3436.

(41) Xu, W.; Wang, D.; Tang, B. Z., NIR-II AIEgens: A Win–Win Integration towards Bioapplications. *Angew. Chem. Int. Ed.* **2021**, *60*, 7476-7487.

(42) Yang, Q.; Hu, Z.; Zhu, S.; Ma, R.; Ma, H.; Ma, Z.; Wan, H.; Zhu, T.; Jiang, Z.; Liu, W.; Jiao, L.; Sun, H.; Liang, Y.; Dai, H. Donor Engineering for NIR-II Molecular Fluorophores with Enhanced Fluorescent Performance. *J. Am. Chem. Soc.* **2018**, *140*, 1715-1724.

(43) Tian, R.; Ma, H.; Yang, Q.; Wan, H.; Zhu, S.; Chandra, S.; Sun, H.; Kiesewetter, D. O.; Niu, G.; Liang, Y.; Chen, X. Rational design of a super-contrast NIR-II fluorophore affords high-performance NIR-II molecular imaging guided microsurgery. *Chem. Sci.* **2019**, *10*, 326-332.

(44) Li, Y.; Cai, Z.; Liu, S.; Zhang, H.; Wong, S. T. H.; Lam, J. W. Y.; Kwok, R. T. K.; Qian, J.; Tang, B. Z. Design of AIEgens for near-infrared IIb imaging through structural modulation at molecular and morphological levels. *Nat. Commun.* **2020**, *11*, 1255.

(45) Liu, S.; Chen, R.; Zhang, J.; Li, Y.; He, M.; Fan, X.; Zhang, H.; Lu, X.; Kwok, R. T. K.; Lin, H.; Lam, J. W. Y.; Qian, J.; Tang, B. Z. Incorporation of Planar Blocks into Twisted Skeletons: Boosting Brightness of Fluorophores for Bioimaging beyond 1500 Nanometer. *ACS Nano* **2020**, *14*, 14228-14239.

(46) Liu, S.; Ou, H.; Li, Y.; Zhang, H.; Liu, J.; Lu, X.; Kwok, R. T. K.; Lam, J. W. Y.; Ding, D.; Tang, B. Z. Planar and Twisted Molecular Structure Leads to the High Brightness of Semiconduct-

ing Polymer Nanoparticles for NIR-IIa Fluorescence Imaging. *J. Am. Chem. Soc.* **2020**, *142*, 15146-15156.

(47) Liu, S.; Chen, C.; Li, Y.; Zhang, H.; Liu, J.; Wang, R.; Wong, S. T. H.; Lam, J. W. Y.; Ding, D.; Tang, B. Z. Constitutional Isomerization Enables Bright NIR‐II AIEgen for Brain‐Inflammation Imaging. *Adv. Funct. Mater.* **2019**, *30*, 1908125.

(48) Qi, J.; Li, J.; Liu, R.; Li, Q.; Zhang, H.; Lam, J. W. Y.; Kwok, R. T. K.; Liu, D.; Ding, D.; Tang, B. Z. Boosting Fluorescence-Photoacoustic-Raman Properties in One Fluorophore for Precise Cancer Surgery. *Chem* **2019**, *5*, 2657-2677.

(49) Qi, J.; Sun, C.; Li, D.; Zhang, H.; Yu, W.; Zebibula, A.; Lam, J. W. Y.; Xi, W.; Zhu, L.; Cai, F.; Wei, P.; Zhu, C.; Kwok, R. T. K.; Streich, L. L.; Prevedel, R.; Qian, J.; Tang, B. Z. Aggregation-Induced Emission Luminogen with Near-Infrared-II Excitation and Near-Infrared-I Emission for Ultradeep Intravital Two-Photon Microscopy. *ACS Nano* **2018**, *12*, 7936-7945.

(50) Qi, J.; Sun, C.; Zebibula, A.; Zhang, H.; Kwok, R. T. K.; Zhao, X.; Xi, W.; Lam, J. W. Y.; Qian, J.; Tang, B. Z. Real-Time and High-Resolution Bioimaging with Bright Aggregation-Induced Emission Dots in Short-Wave Infrared Region. *Adv. Mater.* **2018**, *30*, 1706856.

(51) Shuai, Z.; Peng, Q., Organic light-emitting diodes: theoretical understanding of highly efficient materials and development of computational methodology. *National Science Review* **2017**, *4*, 224-239.

(52) Carlson, L. J.; Maccagnano, S. E.; Zheng, M.; Silcox, J.; Krauss, T. D. Fluorescence Efficiency of Individual Carbon Nanotubes. *Nano Lett.* 2007, **7**, 3698-3703.

(53) Xie, W.; Deng, W.-W.; Zan, M.; Rao, L.; Yu, G.-T.; Zhu, D.-M.; Wu, W.-T.; Chen, B.; Ji, L.-W.; Chen, L.; Liu, K.; Guo, S.-S.; Huang, H.-M.; Zhang, W.-F.; Zhao, X.; Yuan, Y.; Dong, W.; Sun, Z.-J.; Liu, W. Cancer Cell Membrane Camouflaged Nanoparticles to Realize Starvation Therapy Together with Checkpoint Blockades for Enhancing Cancer Therapy. *ACS Nano* 2019, **13**, 2849-2857

(54) Jiang, R.; Dai, J.; Dong, X.; Wang, Q.; Meng, Z.; Guo, J.; Yu, Y.; Wang, S.; Xia, F.; Zhao, Z.; Lou, X.; Tang, B. Z. Improving Image-Guided Surgical and Immunological Tumor Treatment Efficacy by Photothermal and Photodynamic Therapies Based on a Multifunctional NIR AIEgen. *Adv. Mater.* **2021**, *33*, 2101158.

(55) Liang, J. L.; Luo, G. F.; Chen, W. H.; Zhang, X. Z. Recent Advances in Engineered Materials for Immunotherapy-Involved Combination Cancer Therapy. *Adv. Mater.* **2021**, 10.1002/adma.202007630.

Donor/π-Bridge Manipulation for Constructing a Stable NIR-II Aggregation-Induced Emission Luminogen with Balanced Phototheranostic Performance.

Insert Table of Contents artwork here